

Rodrigues LFS, Sarson GR, Shukurov A, Bushby PJ, Fletcher A.

[The Parker instability in disk galaxies.](#)

The Astrophysical Journal 2016, 816(1), 2

Copyright:

This is the authors accepted manuscript of an article that was published in its final definitive form by IOP publishing, 2016

DOI link to article:

<http://dx.doi.org/10.3847/0004-637X/816/1/2>

Date deposited:

10/02/2016

Embargo release date:

21 December 2016



This work is licensed under a [Creative Commons Attribution-NonCommercial 3.0 Unported License](#)

THE PARKER INSTABILITY IN DISK GALAXIES

L. F. S. RODRIGUES,¹ G. R. SARSON,¹ A. SHUKUROV,¹ P. J. BUSHBY,¹ AND A. FLETCHER¹

School of Mathematics and Statistics, Newcastle University, Newcastle upon Tyne, NE1 7RU, UK

Draft version 958. Last update by nlfsr on 01-11-2015 at 21:09 (GMT+0000).

ABSTRACT

We examine the evolution of the Parker instability in galactic disks using 3D numerical simulations. We consider a local Cartesian box section of a galactic disk, where gas, magnetic fields and cosmic rays are all initially in a magnetohydrostatic equilibrium. This is done for different choices of initial cosmic ray density and magnetic field. The growth rates and characteristic scales obtained from the models, as well as their dependences on the density of cosmic rays and magnetic fields, are in broad agreement with previous (linearized, ideal) analytical work. However, this non-ideal instability develops a multi-modal 3D structure, which cannot be quantitatively predicted from the earlier linearized studies. This 3D signature of the instability will be of importance in interpreting observations. As a preliminary step towards such interpretations, we calculate synthetic polarized intensity and Faraday rotation measure maps, and the associated structure functions of the latter, from our simulations; these suggest that the correlation scales inferred from rotation measure maps are a possible probe for the cosmic ray content of a given galaxy. Our calculations highlight the importance of cosmic rays in these measures, making them an essential ingredient of realistic models of the interstellar medium.

Keywords: instabilities, galaxies: ISM, ISM: cosmic rays, ISM: magnetic fields

1. INTRODUCTION

The magnetic buoyancy (or magnetic Rayleigh–Taylor) instability enhanced by cosmic rays in disk galaxies is known as the Parker instability (Parker 1966, 1967, 1969). Since cosmic rays are practically weightless but exert pressure comparable to that of thermal gas, turbulence and magnetic fields, their effect on the instability is significant. The growth rate of the most unstable mode is of the order of the Alfvén crossing time, $\tau_A = h/c_A \simeq 10^7$ yr, based on the disk scale height $h = 100$ pc, and assuming an Alfvén speed of $c_A = 10$ km s^{−1}; the corresponding wavelength is of order 1 kpc (Parker 1979). The nature of the instability is quite generic and it is therefore expected to occur in all magnetized astrophysical disks, including accretion disks and spiral galaxies. The saturation mechanism of the instability and the resulting state of the system are not well understood. As discussed by Foglizzo & Tagger (1994, 1995), differential rotation weakens the instability. Gas viscosity, random magnetic fields and finite cosmic ray diffusion also suppress it (Kuznetsov & Ptuskin 1983), as they interfere with the sliding of the gas to the bottom of magnetic loops as well as the streaming of cosmic rays to the top of these loops.

There have been several studies of the Parker instability using linear perturbation theory. Giz & Shu (1993) extended the initial works by Parker by employing a more realistic vertical gravitational acceleration, $g_z(z) \propto \tanh z$, which is continuous across the Galactic midplane, rather than the step-function $|g_z(z)| = \text{constant}$ that was previously used. This allowed them to consider the vertical symmetry of the instability and identify a family of unstable modes that cross the midplane (in which case the vertical velocity, U_z , and the vertical magnetic field, B_z , are not identically zero at $z = 0$). Modes of

this type, which are often referred to as ‘antisymmetric’, were also found by Horiuchi et al. (1988), although they used a different gravitational acceleration, $g(z) \propto z/(r_0^2 + z^2)^{3/2}$. (The issue of symmetry about the midplane is discussed in detail in section 3.2.) Kim & Hong (1998) showed that the use of a more realistic gravity profile also results in a faster growth rate and shorter horizontal wavelength for the instability. Ryu et al. (2003) included the effects of finite cosmic ray diffusion; the previous works had taken the diffusivity to be infinite along the magnetic field and zero perpendicular to it. Their linear analysis found that the finite, but large, parallel diffusivity of cosmic rays in the interstellar medium (ISM) is well approximated by infinite-diffusivity models, and that the perpendicular diffusivity has no significant effect. Kuwabara & Ko (2006) studied Parker-Jeans instabilities in the ISM using a model which does not have an external gravitational field but does include self-gravity. They confirmed that higher cosmic ray diffusivity results in faster growth rates, and that modes with a wavevector parallel to the magnetic field direction are least stable.

There have also been many numerical studies of the Parker instability. To date most numerical models have been ideal: the terms involving the gas viscosity in the Navier-Stokes equation, and the magnetic diffusivity in the magnetic induction equation, are set to zero; notable exceptions are Hanasz et al. (2002) and Tanuma et al. (2003), which did include finite resistivity. Numerical models have generally assumed that the vertical gravity is uniform and discontinuous at the midplane and/or do not include cosmic rays. Matsumoto et al. (1988) and Basu et al. (1997) used 2D simulations to investigate the nonlinear evolution of the instability, and showed that the midplane crossing modes dominate. Kim et al. (1998) found that filamentary or sheetlike structures formed when the system approaches a new equilibrium after 10^9 yr in 3D models. Disk rotation was included in the 3D simulations of Chou et al. (1997) and Kim et al. (2001), who showed that the Coriolis force results in a twisting of the magnetic loops and may also help to randomize the initially uniform magnetic field.

¹ luiz.rodrigues@newcastle.ac.uk (LFSR),
graeme.sarson@newcastle.ac.uk (GRS),
anvar.shukurov@newcastle.ac.uk (AS),
paul.bushby@newcastle.ac.uk (PJB),
andrew.fletcher@newcastle.ac.uk (AF).

3D models including self-gravity and differential rotation, allowing for the development of Jeans and swing instabilities as well as the Parker instability, were used by Kim et al. (2002) to show that a mixture of midplane symmetric and midplane crossing modes can develop in the ISM. The above simulations all excluded a cosmic ray component, which was added by Hanasz & Lesch (2000, 2003) in 3D, to investigate the triggering of the Parker instability by a supernova remnant, and by Kuwabara et al. (2004), who used 2D MHD simulations to confirm the connection between cosmic ray diffusivity and the Parker instability growth rate found in their earlier linear analysis. Mouschovias et al. (2009) allowed for phase transitions in a 2D MHD model (without cosmic rays), found that the midplane crossing mode was favoured, and argued that a non-linear triggering of the Parker instability by a spiral density shock-front could allow the instability to form gas clouds on a timescale compatible with observations.

The instability produces buoyant loops of a large-scale magnetic field at a kiloparsec scale. These ‘Parker loops’ are expected to lie largely in the azimuthal direction (the direction of the large-scale field). This corresponds to the ‘undular’ modes (with wavevector parallel to magnetic field \mathbf{B}) which are expected to dominate over the ‘interchange’ modes (with wavevector perpendicular to \mathbf{B}) in most linear analyses (see, e.g. Matsumoto et al. 1993, for a discussion of these modes). (Indeed, some authors identify the Parker instability specifically with these undular modes, rather than simply in terms of the fundamental buoyancy mechanism.) There have been numerous attempts to detect such Parker loops in observations, but they have met with little success². This may be surprising, since the instability is strong and generic. Therefore, we consider here the detailed development and possible observational consequences of the instability in galactic disks.

We simulate the evolution of a simple model of a section of a galactic disk, where gas, magnetic fields and cosmic rays evolve in the gravitational field of stars and dark matter halo. Cosmic rays are described in the advection-diffusion approximation with a diffusion tensor aligned with the local magnetic field. The simulation setup is aimed at facilitating comparisons with previous analytical works, as well as capturing clear signatures of the Parker instability which can later be compared to more advanced simulations and observations. For these reasons, we use the isothermal approximation (where there is no possibility of confusion with thermally-driven instabilities), and omit rotation and rotational shear (to avoid any confusion with other instabilities, such as the magneto-rotational instability). We also refrain from using any source terms for the magnetic field and the cosmic ray energy density, since this could lead to artificial spatial biases.

This paper is organized as follows. In Section 2 the model is described in detail. In Section 3 the results are presented: in §3.1 we find the growth rates and typical wavenumbers associated with the instability, as well as the dependence on the density of cosmic rays and the strength of the magnetic field; in §3.2 we examine the symmetries of the instability, and the variation of the growth rates with height; in §3.3 we address the dependence on the choice of diffusivities; and in §3.4 we study possible observable signatures: namely the prospects of

observing Parker loops from synchrotron emission of edge-on galaxies, or from the Faraday rotation measure signal from face-on galaxies. Finally, in Section 4 we state our conclusions.

2. MODEL DESCRIPTION

All the numerical calculations in this work were performed using the open source, high-order finite difference PENCIL code³, designed for fully non-linear, compressible magnetohydrodynamic simulations. The cosmic ray calculations employed the COSMICRAY and COSMICRAYFLUX modules (Snodin et al. 2006).

2.1. Basic equations and cosmic ray modeling

We solve equations for mass conservation, momentum, and magnetic induction, for an isothermal gas assuming constant kinematic viscosity ν and magnetic diffusivity η :

$$\frac{D \ln \rho}{Dt} = -\nabla \cdot \mathbf{U}, \quad (1)$$

$$\frac{D \mathbf{U}}{Dt} = \mathbf{g} - \frac{\nabla(p_g + p_{cr})}{\rho} + \frac{\mathbf{j} \times \mathbf{B}}{\rho} + \nu [\nabla^2 \mathbf{U} + \frac{1}{3} \nabla (\nabla \cdot \mathbf{U}) + 2 \mathbb{W} \cdot \nabla \ln \rho], \quad (2)$$

$$\frac{\partial \mathbf{A}}{\partial t} = \mathbf{U} \times \mathbf{B} + \eta \nabla^2 \mathbf{A}, \quad (3)$$

where ρ is the gas density, \mathbf{U} is the gas velocity, \mathbf{A} is the magnetic vector potential, $\mathbf{B} = \nabla \times \mathbf{A}$ is the magnetic field (with $\nabla \cdot \mathbf{B} = 0$ by construction), $\mathbf{j} = \nabla \times \mathbf{B} (c/4\pi)$ is the electric current density, with c the speed of light in vacuum, \mathbb{W} is the rate of strain tensor,

$$W_{ij} = \frac{\partial U_i}{\partial x_j} + \frac{\partial U_j}{\partial x_i} - \frac{2}{3} \delta_{ij} \nabla_k U_k,$$

$p_g = \rho c_s^2$ is the gas pressure, c_s is the adiabatic speed of sound, p_{cr} is the cosmic ray pressure and \mathbf{g} is the gravitational acceleration. We neglect the effects of rotation and rotational shear.

Cosmic rays are modeled using a fluid approximation (e.g. Parker 1969; Schlickeiser & Lerche 1985) where the cosmic ray energy density ϵ_{cr} is governed by

$$\frac{\partial \epsilon_{cr}}{\partial t} + \nabla \cdot (\epsilon_{cr} \mathbf{U}) + p_{cr} \nabla \cdot \mathbf{U} = -\nabla \cdot \mathbf{F}, \quad (4)$$

with \mathbf{F} the cosmic ray flux defined below. The cosmic ray pressure that appears in equation (2) is obtained from the equation of state

$$p_{cr} = \epsilon_{cr} (\gamma_{cr} - 1),$$

with γ_{cr} the cosmic ray adiabatic index. We adopt $\gamma_{cr} = 4/3$, as appropriate for the ultrarelativistic gas; other values in the range $4/3 \leq \gamma_{cr} \leq 5/3$ are possible, with the latter value being relevant for non-relativistic particles (Schlickeiser & Lerche 1985).

The cosmic ray flux \mathbf{F} is introduced in a non-Fickian form justified and discussed by Snodin et al. (2006),

$$\tau \frac{\partial F_i}{\partial t} = -\kappa_{ij} \nabla_j \epsilon_{cr} - F_i, \quad (5)$$

² Recently, magnetic loops and filaments have been detected in WMAP and Planck data (Vidal et al. 2015; Planck Collaboration et al. 2015). However, these are likely a consequence of interstellar turbulence driven by supernovae remnants (Planck Collaboration et al. 2015, 2014; Mertsch & Sarkar 2013) and not of Parker instability.

³ Documentation and download instructions can be found at <http://pencil-code.nordita.org/>.

where τ can be identified with the decorrelation time of the cosmic ray pitch angles, and κ is the diffusion tensor,

$$\kappa_{ij} = \kappa_{\perp} \delta_{ij} + (\kappa_{\parallel} - \kappa_{\perp}) \hat{B}_i \hat{B}_j, \quad (6)$$

where a circumflex denotes a unit vector. When τ is negligible, equation (5) reduces to the Fickian diffusion flux, but the large diffusivity of cosmic rays makes the non-Fickian effects both physically significant and numerically useful. When τ is finite, the propagation speed of cosmic rays remains finite (e.g., Bakunin 2008). This prescription also avoids the possibility of singularities at X-type magnetic null points where κ_{ij} is undefined (Snodin et al. 2006).

For numerical solution, the maximum time step δt for the cosmic ray physics might be constrained either by an advective-style Courant condition based on the cosmic ray flux equation (5), or by a diffusive-style Courant condition based on the cosmic ray energy density equation (4). (The latter would be appropriate for the Fickian case $\tau = 0$.) I.e. we might constrain $\delta t \leq C_{\text{adv}} \delta z / c_{\text{cr}}$, or $\delta t \leq C_{\text{diff}} \delta z^2 / \kappa_{\parallel}$, with δz the smallest numerical grid spacing, and $c_{\text{cr}} = (\kappa_{\parallel} / \tau)^{1/2}$ the characteristic speed for the cosmic ray diffusion along the local magnetic field; here C_{adv} and C_{diff} are empirical constants. For similar advective and diffusive processes in the other equations (based on speeds c_s , c_A , U , and diffusivities ν , η , respectively), we adopt the constants $C_{\text{adv}} = 0.4$, $C_{\text{diff}} = 0.06$. For the relatively large value of κ_{\parallel} used in the following, this value of C_{diff} results in a significant reduction of δt , to a value which numerical experiments show to be unnecessarily small. I.e. an appropriate empirical value of C_{diff} for the cosmic ray diffusion would be significantly greater than our standard value of 0.06. (This is perhaps unsurprising, given the anisotropic nature of our cosmic ray diffusion; κ_{\parallel} only applies along magnetic field lines, where cosmic ray energy density gradients tend to be small.) On the other hand, our standard value of $C_{\text{adv}} = 0.4$ results in an appropriate constraint for δt (allowing the cosmic ray physics to control the timestep when necessary, but avoiding unnecessarily small timesteps), and achieves this without the introduction of an additional empirical constant. In the calculations reported here, we use this advective-style constraint.

2.2. Numerical domain and initial conditions

We use a local Cartesian box to represent a portion of the galactic disk, with x , y and z representing the radial, azimuthal and vertical directions, respectively. The domain is of size $6\text{kpc} \times 12\text{kpc} \times 3.5\text{kpc}$ in the x , y and z directions, with the galactic midplane at the center of the vertical range $-1.75\text{kpc} \leq z \leq 1.75\text{kpc}$. We use a grid of $256 \times 512 \times 315$ mesh points, so have the numerical grid spacings $(\delta_x, \delta_y, \delta_z) \approx (23.4\text{ pc}, 23.4\text{ pc}, 11.1\text{ pc})$. The height of the domain has been chosen to be much larger than the characteristic vertical scale of the instability (see below).

The initial state is an isothermal disk under magnetohydrostatic equilibrium in an external gravity field with the gravitational acceleration given by

$$g_z(z) = -2\pi G \Sigma \tanh\left(\frac{z}{h}\right), \quad (7)$$

where $h = 500\text{pc}$ is the scale height of warm gas, $\Sigma = 100\text{M}_{\odot}\text{pc}^{-2}$ is the total surface mass density of the disk, and G is Newton's gravitational constant.

The relative contributions of the gas, magnetic and cosmic ray to the total pressure in the initial state are parameterized

using

$$\alpha = \frac{p_B}{p_g} \quad \text{and} \quad \beta = \frac{p_{\text{cr}}}{p_g}, \quad (8)$$

where $p_B = B^2/(8\pi)$ is the magnetic pressure. The initial state is unstable for any values $\alpha + \beta > \gamma_g - 1 = 0$ (where $\gamma_g = 1$ is the adiabatic index of the gas).

The temperature of the gas follows as

$$T = \frac{\pi G \Sigma m_p \mu h}{k_B (1 + \alpha + \beta)}, \quad (9)$$

where m_p is the proton mass, μ is the mean molecular mass (here $\mu = 1$), and k_B is Boltzmann's constant. Under magnetohydrostatic equilibrium with the gravity field adopted, the initial gas density is given by

$$\rho(z) = \frac{\Sigma_g}{2h} \text{sech}^2\left(\frac{z}{h}\right), \quad (10)$$

where Σ_g is the gas surface density.

When the pressure scale heights of magnetic field and cosmic rays are identical, as imposed by equation (8), the initial energy density distribution of cosmic rays is

$$\varepsilon_{\text{cr}}(z) = \frac{\pi G \Sigma \Sigma_g}{2(\gamma_{\text{cr}} - 1)} \text{sech}^2\left(\frac{z}{h}\right) \frac{\beta}{1 + \alpha + \beta}. \quad (11)$$

The initial magnetic field, assumed to be azimuthal, is obtained from

$$A_x = 4\pi h \left(\frac{G \Sigma \Sigma_g \alpha}{1 + \alpha + \beta} \right)^{1/2} \arctan \left[\tanh\left(\frac{z}{2h}\right) \right], \quad (12)$$

$$A_y = A_z = 0,$$

which leads to

$$B_y^2 = 4\pi^2 G \Sigma \Sigma_g \text{sech}^2\left(\frac{z}{h}\right) \frac{\alpha}{1 + \alpha + \beta}, \quad (13)$$

$$B_x^2 = B_z^2 = 0.$$

This initial state is not in exact magnetohydrostatic equilibrium, except for $\alpha = \beta = 0$, due to the magnetic diffusion and perpendicular cosmic ray diffusion. For the parameters used, the diffusive time scales are much longer than the timescale of the Parker instability, so any diffusive evolution of the initial state is inconsequential (see Section 2.4).

The initial state is perturbed by noise in the velocity field: at each mesh point a random velocity was specified with a magnitude uniformly distributed in the range $0 \leq U \leq 14 \text{sech}^2(z/h) \text{ km s}^{-1}$. The velocity perturbation is subsonic, with the rms value of order 1 km s^{-1} throughout the domain. This value was chosen to avoid unnecessarily long transients in the onset of the instability (during which time the initial state might evolve significantly), while avoiding directly driving the instability.

2.3. Boundary conditions

We assume periodicity at the horizontal (x and y) boundaries. The height of the domain, $Z_0 = 1.75\text{kpc}$, is much larger than the characteristic vertical scale of the instability, so that the precise boundary conditions at the top and bottom of the domain do not significantly affect the results; these are adopted as follows. Symmetry about the top and bottom

Table 1
Various timescales of the problem, with respect to vertical disk crossing times.

Time scale	Definition	Magnitude
Sound speed	$\tau_s = \frac{h}{c_s} = \left(\frac{h}{\gamma_g \pi G \Sigma} \right)^{1/2} (1 + \alpha + \beta)^{1/2}$	$26.6 \text{ Myr} \left(\frac{1 + \alpha + \beta}{2} \right)^{1/2}$
Alfvén speed ^a	$\tau_A = \frac{h}{c_A} = \left(\frac{h}{2\pi G \Sigma} \right)^{1/2} \left(\frac{1 + \alpha + \beta}{\alpha} \right)^{1/2}$	$18.8 \text{ Myr} \left(\frac{1 + \alpha + \beta}{2\alpha} \right)^{1/2}$
Viscous	$\tau_v = \frac{h^2}{\nu}$	2.39 Gyr
Magnetic diffusion	$\tau_\eta = \frac{h^2}{\eta}$	4.77 Gyr
Cosmic ray parallel diffusion	$\tau_{\text{cr},\parallel} = \frac{h^2}{\kappa_\parallel}$	4.77 Myr
Cosmic ray perpendicular diffusion	$\tau_{\text{cr},\perp} = \frac{h^2}{\kappa_\perp}$	2.39 Gyr
Cosmic ray flux propagation speed ^b	$\tau_{\text{cr},\tau} = \frac{h}{c_{\text{cr}}} = h / \sqrt{\kappa_\parallel / \tau}$	6.91 Myr

^aInitial value.

^bBased on parallel diffusion.

Table 2
Values of parameters adopted

Quantity	Symbol	Value
Disk gas surface density	Σ_g	$10 \text{ M}_\odot \text{ pc}^{-2}$
Disk total surface density	Σ	$100 \text{ M}_\odot \text{ pc}^{-2}$
Disk scale-height	h	0.5 kpc
CR flux correlation time	τ	10 Myr
Kinematic viscosity	ν	$3.16 \times 10^{25} \text{ cm}^2 \text{ s}^{-1}$
Magnetic diffusivity	η	$1.58 \times 10^{25} \text{ cm}^2 \text{ s}^{-1}$
CR parallel diffusivity	κ_\parallel	$1.58 \times 10^{28} \text{ cm}^2 \text{ s}^{-1}$
CR perpendicular diffusivity	κ_\perp	$3.16 \times 10^{25} \text{ cm}^2 \text{ s}^{-1}$

boundaries is imposed for U_x and U_y , and antisymmetry for U_z :

$$\frac{\partial U_x}{\partial z} = \frac{\partial U_y}{\partial z} = U_z = 0 \quad \text{at } |z| = Z_0, \quad (14)$$

making these boundaries impenetrable and stress free. The magnetic vector potential is symmetric for A_z , antisymmetric for A_y and generalized antisymmetric for A_x :

$$\frac{\partial^2 A_x}{\partial z^2} = A_y = \frac{\partial A_z}{\partial z} = 0 \quad \text{at } |z| = Z_0. \quad (15)$$

These conditions are similar to those for a perfectly conducting boundary (which would require $A_x = 0$), but the condition of antisymmetry in A_x has been relaxed to avoid overly distorting the initial background profile $A_x(z)$. Similarly, to minimize distortions to the initial background density profile, generalized antisymmetry is imposed on $\ln \rho$ at the top and bottom of the domain:

$$\frac{\partial^2 \ln \rho}{\partial z^2} = 0 \quad \text{at } |z| = Z_0. \quad (16)$$

This condition has no obvious physical interpretation but it places no strong constraints on the density distribution. The cosmic ray energy density and flux at the top and bottom

boundaries satisfy

$$\frac{\partial \epsilon_{\text{cr}}}{\partial z} = 0, \quad \frac{\partial F_x}{\partial z} = \frac{\partial F_y}{\partial z} = F_z = 0, \quad (17)$$

which corresponds to vanishing vertical flux in the Fickian limit.

The boundary conditions have been chosen largely for simplicity. Because of the impenetrability of the surface of the domain, there could in principle be reflection of waves and/or the artificial accumulation of buoyant material, but no such problems emerged in the results reported below (which focus primarily upon the early phases of evolution of the Parker instability). We have also rerun one of our simulations in a domain with larger vertical size to confirm that the domain is large enough to prevent spurious boundary effects over the timescales explored (see appendix A).

2.4. Parameters and timescales

The parameters used, including our fiducial choices of the various diffusivities involved, are shown in table 2; the resulting timescales of interest for our disk are shown in table 1. These values of Σ and Σ_g correspond to an initial midplane gas density of $\rho(0) = 6.8 \times 10^{-25} \text{ g cm}^{-3}$; for $\alpha = 1$, $\beta = 1$, the corresponding initial azimuthal field strength is $B_y(0) \approx 6 \mu\text{G}$ and the cosmic ray energy density, $\epsilon_{\text{cr}}(0) \approx 4.6 \times 10^{-13} \text{ erg cm}^{-3}$.

Our choice of $\tau = 10 \text{ Myr}$ for the cosmic ray flux correlation timescale ensures that it is smaller than the characteristic timescale of the Parker instability (see Section 3), as well as the sound and Alfvén speed timescales (see table 1). The impact of choosing smaller values for τ was examined, and confirmed to have negligible impact on the results. This value of τ , together with our other choices of parameters, results in the Strouhal number associated with the cosmic ray flux, $\text{St} = c_{\text{cr}} \tau / h = \sqrt{\kappa_\parallel \tau} / h \approx 1.45$, being of order 1. (And note that this estimate, involving parallel diffusivity with the vertical scale height, is arguably an overestimate. Typical horizontal lengthscales are longer than h ; see Section 3.1, below.) Thus we do not expect wavelike behaviour in these simulations; the diffusion of cosmic rays does not differ significantly

from Fickian diffusion.

Our fiducial choices of kinematic viscosity ν and magnetic diffusivity η correspond to a magnetic Prandtl number $\text{Pm} = \nu/\eta = 2$; the effects of varying magnetic Prandtl number are investigated in Section 3.3. The values adopted for ν and η are very significantly larger than expected molecular values (and the resulting $\text{Pm} \sim \mathcal{O}(1)$ is very much smaller than the galactic regime associated with molecular values, $\text{Pm} \gg 1$); but if considered as effective turbulent diffusivities, the values are reasonable.

The parallel cosmic ray diffusivity used is close to the best estimates for this parameter (Ryu et al. 2003; Strong & Moskalenko 1998). The timescales associated with cosmic ray diffusion along the fieldlines ($\tau_{\text{cr},\parallel}$ and $\tau_{\text{cr},\tau}$ in table 1) are significantly shorter than the timescales of the Parker instability, and the sound and Alfvén speed timescales; we are therefore in a reasonable regime for modelling galactic disks, yet may expect some deviations from those analytic results obtained on the basis of infinitely fast propagation of cosmic rays along fieldlines.

The perpendicular diffusivity of cosmic rays, on the other hand, was somewhat reduced from expected values to avoid the escape of the cosmic ray energy density before the development of the instability. As noted in Section 2.2, the initial state will evolve under the diffusion of magnetic field and the perpendicular diffusion of cosmic rays; but the timescales for these processes, 4.77 Gyr and 2.39 Gyr, are very long compared to the other timescales of interest, making the slow diffusive evolution of the background state insignificant.

3. RESULTS AND DISCUSSION

Three-dimensional renderings of the runs of the simulation with $(\alpha, \beta) = (1, 0)$ and $(\alpha, \beta) = (1, 1)$ are shown in Figure 1, in panels (a) and (b) respectively. The images show the snapshots when the kinetic energy in each simulation matched the thermal energy (which is fixed due to the isothermal condition); this corresponds to simulation time 330 Myr for the case without cosmic rays (panel a) and 200 Myr for the case of equal pressure contribution of cosmic rays, magnetic fields and thermal pressure (panel b).

As expected (and as quantified further below), one can see that the presence of cosmic rays leads to an increased number of substructures in the density field. The magnetic field lines, in green, display the characteristic ‘Parker loops’, which also clearly span smaller length scales in the case with cosmic rays.

3.1. Dependence on magnetic and cosmic ray pressures (α and β)

In Figure 2, the time evolution of the root-mean-square velocity U_{rms} , and of the kinetic energy E_{kin} , are shown for different choices of α and β . A period of exponential growth, associated with the development of the instability, can be clearly identified. Increases in the pressure ratio of magnetic fields, α , and of cosmic rays, β , enhance the instability, leading to larger growth rates.

The dependence of the growth rate of U_z , Γ , on α and β is examined in Figure 3, where it is compared with the analytical results of Giz & Shu (1993, GS93) and Ryu et al. (2003, R+03). Under the assumption of equipartition of initial magnetic pressure ($\alpha = 1$), the growth rate increases almost linearly with cosmic ray pressure contribution, from 20.4 Gyr^{-1} , at $\beta = 0$, to 26.0 Gyr^{-1} , at $\beta = 1$. To compare our find-

ings to previous analytical results, one has to take into account the effect of a finite vertical domain with impenetrable boundaries, which limits the maximum vertical wavelength of the perturbation, λ_z . In order to illustrate this, we show three sets of analytic growth rate curves for different choices of λ_z . For arbitrarily large vertical wavelengths GS93 predict fastest growing modes with growth rates 28.6 Gyr^{-1} and 52.8 Gyr^{-1} at $\beta = 0, 1$, respectively, which differ significantly from our results. If, instead, the maximum attainable vertical wavelength in our domain is considered, $\lambda_z = 3.5 \text{ kpc}$, the growth rates are closer to what is obtained in the simulations. For the $\beta = 0$ case (i.e. the run without cosmic rays), there is good quantitative agreement between the model and GS93. However, the slope, $d\Gamma/d\beta$, found from the simulation results is clearly smaller. It should be noted that GS93 assumes infinite diffusion of cosmic rays parallel to the field and no perpendicular diffusion, and both of these factors would lead us to expect smaller growth rates (Ryu et al. 2003).

The analytical results of Ryu et al. (2003), which take into account finite cosmic ray diffusivity, give a better match for the slope $d\Gamma/d\beta$, but have smaller growth rates because of the assumption of a constant gravitational field; the importance of the gravity profile in this respect is clear from Kim & Hong (1998), who considered uniform, linear and ‘realistic’ fields (the latter being similar to our own).

In the lower panel of Figure 3, the weaker dependence of the growth rate on α is shown, for a fixed $\beta = 0.25$. This relatively weak dependence is expected for realistic gravity fields (Kim & Hong 1998), but highlights the importance of cosmic rays (and the importance of realistic background states) for this instability.

Of particular interest are the disturbances to the initial state of the system defined in Section 2.2. These can be expressed in terms of dimensionless quantities, defined as

$$s(z) = \frac{\rho(z) - \rho_0(z)}{\rho_0(z)}, \quad (18)$$

$$\mathbf{u}(z) = \frac{\mathbf{U}(z)}{c_s}, \quad (19)$$

$$\mathbf{b}(z) = \frac{\mathbf{B}(z) - \mathbf{B}_0(z)}{B_{0,y}(z)}, \quad (20)$$

$$e_{\text{cr}}(z) = \frac{\epsilon_{\text{cr}}(z) - \epsilon_{\text{cr},0}(z)}{\epsilon_{\text{cr},0}(z)}, \quad (21)$$

where the subscript 0 denotes the quantity at $t = 0$. These have the same form as the perturbations defined by Giz & Shu (1993) and provide an estimate for the degree of non-linearity of the system.

In Figure 4 slices at constant height ($z = 0.5 \text{ kpc}$, i.e. one scale-height away from the midplane) are shown for different choices of β . The selected snapshots correspond to the instant when the kinetic energy in the domain reaches 70 per cent of thermal energy, to allow comparisons of the spatial structure on an equal footing (i.e. to account for the different timescales of three runs), with the actual time indicated at the top of each column. The system is still in the linear phase (with amplitudes typically being below 20%) but a significant amount of non-trivial structure is already visible. The spatial distribution of the substructures does not change with time⁴, only their amplitudes vary. The observed structures are com-

⁴ For a movie, see <http://doi.org/8j3>.

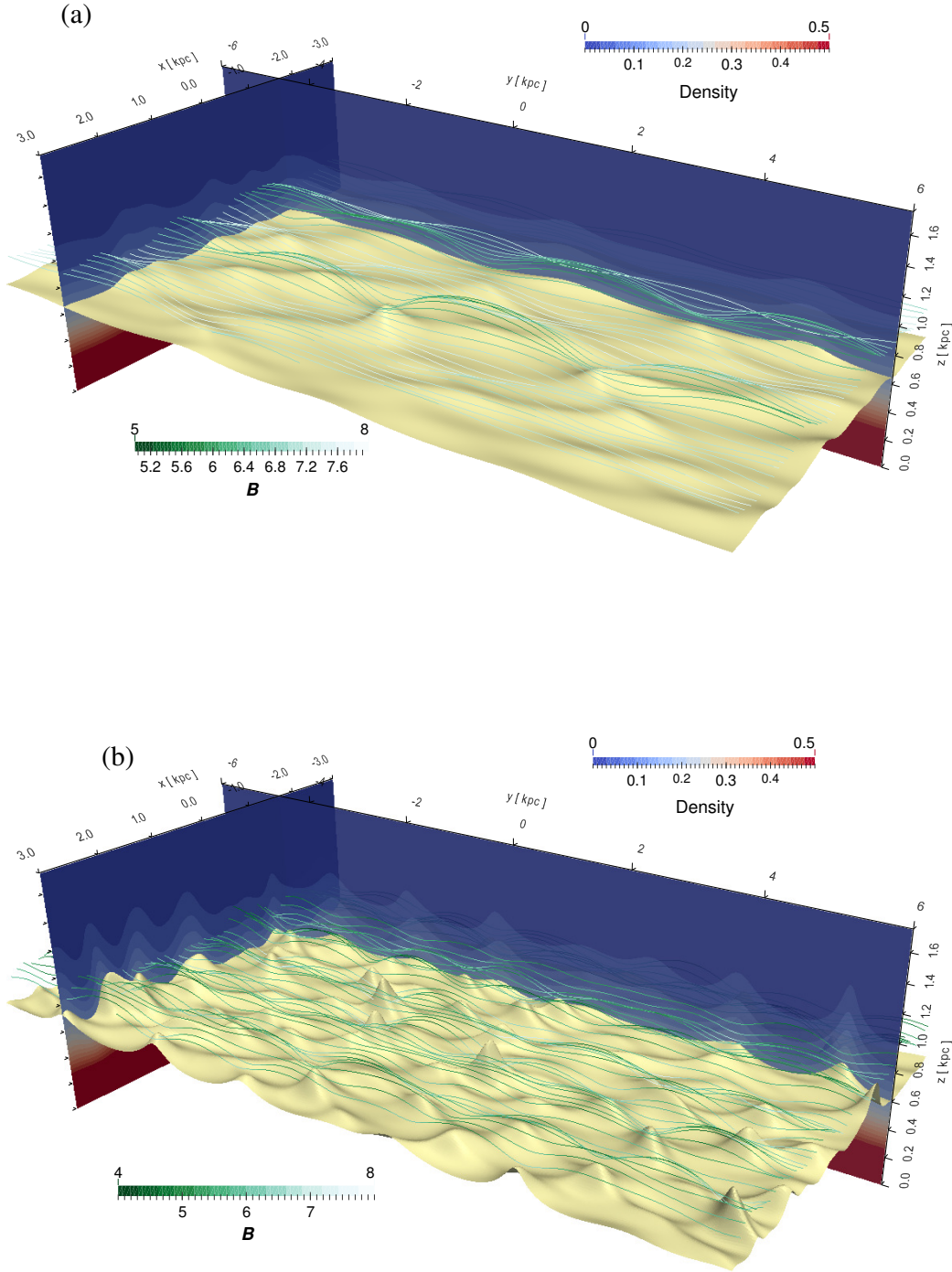


Figure 1. Renderings of the simulations at the time where the kinetic energy is close to the thermal energy. Panel (a) shows the outcome of the choice $\alpha = 1.0$ and $\beta = 0.0$ at $t = 330 \text{ Myr}$. Panel (b) shows the outcome of the choice $\alpha = 1.0$ and $\beta = 1.0$ at $t = 200 \text{ Myr}$. The yellow surface corresponds to a density of $1.5 \times 10^{-25} \text{ g cm}^{-3}$. The green lines represent magnetic field lines, color-coded by field magnitude following the color-bar in the plots, which is units of $0.35 \mu\text{G}$. The slices show the density in units of $10^{-24} \text{ g cm}^{-3}$. Only the top half (i.e. the volume between the midplane and the top boundary) of the simulation domain is shown.

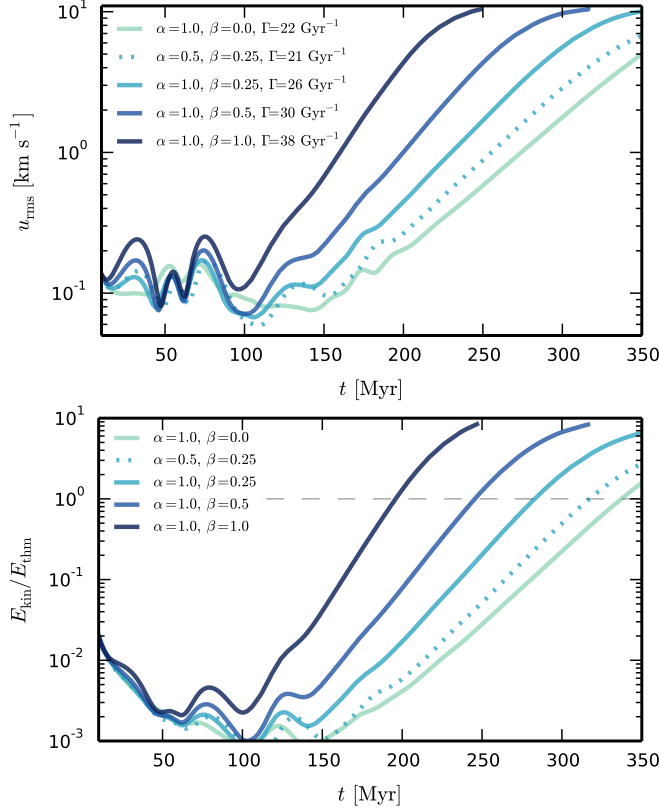


Figure 2. The top panel shows the evolution of the the root mean square of the velocity, U_{rms} , for selected choices of α and β as indicated. The bottom panel shows the evolution of the kinetic energy in the whole simulation box (normalised by the fixed thermal energy). The horizontal dashed line corresponds to equipartition of thermal and kinetic energy; the analysis in the text is for states before this point, when $E_{\text{kin}} = 0.7E_{\text{therm}}$.

prised of over-dense sheets of inflowing gas surrounded by outflowing, magnetized, cosmic ray-rich, under-dense gas.

In Figures 5 and 6, we examine the power spectra of perturbations to the magnetic and velocity field, comparing the cases of $(\alpha, \beta) = (1, 0)$ and $(\alpha, \beta) = (1, 1)$, at the snapshot when $E_{\text{kin}} = 0.7E_{\text{therm}}$. In the absence of cosmic rays, the two dominant modes are $(k_x, k_y) = (1.0 \text{ kpc}^{-1}, 1.6 \text{ kpc}^{-1})$ and $(3.1 \text{ kpc}^{-1}, 2.1 \text{ kpc}^{-1})$. The k_x value of the first mode actually corresponds to the domain size in the x -direction (i.e. $2\pi/L_x$). There is significant spread in k_x , which is consistent with the weak dependence of the growth rate with wavenumber noted in the analytic calculations. There is less spread in k_y however, with energy being concentrated close to the wavenumber associated with the fastest growing mode of [Giz & Shu \(1993\)](#), $k_{y,\text{GS}}$, which is the dotted curve plotted. Our calculations favor slightly smaller wavenumbers (larger wavelengths), which is understandable given the inclusion of non-zero diffusivities.

In the presence of cosmic rays, there is a general decrease of the wavelength along the azimuthal direction. To facilitate the comparison, the two most prominent modes in the $\beta = 1$ case are $(k_x, k_y) = (1.0 \text{ kpc}^{-1}, 2.1 \text{ kpc}^{-1})$ and $(5.2 \text{ kpc}^{-1}, 2.6 \text{ kpc}^{-1})$. While most of the energy is still close to the relevant azimuthal wavenumber from [Giz & Shu \(1993\)](#), $k_y = k_{y,\text{GS}}$ (here plotted as the dashed line), there is more spread, showing that other modes are also being significantly excited. Again, the dominant modes tend to have wavenumbers slightly smaller than the value for the ideal case.

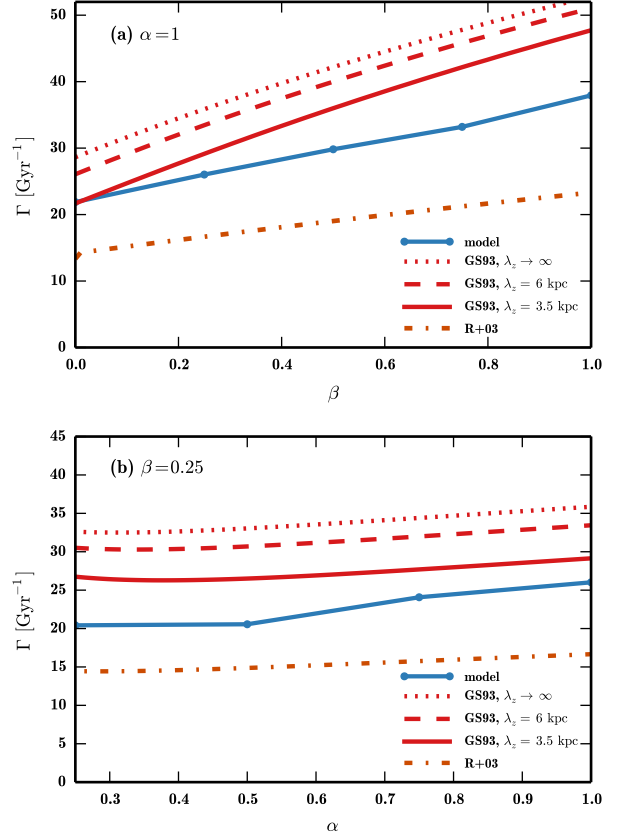


Figure 3. Dependence of the growth rate of the velocity field with pressure ratio. Panel (a): varying cosmic ray pressure ratio, β (with fixed $\alpha = 1$), is shown by solid blue curve. Panel (b): magnetic field pressure ratio, α (with fixed $\beta = 0.25$), is shown by solid blue curve. In both panels, the fastest growing modes computed using the equations derived by [Giz & Shu \(1993, GS93\)](#) correspond to red curves. Different choices for the vertical wavelengths, λ_z , are shown with different line styles, as indicated. The fastest growing modes predicted by [Ryu et al. \(2003, R+03\)](#) are shown by the dash-dotted orange curve.

Closer to the midplane there is less overall power and less relative power in the fastest growing modes; this is discussed in Section 3.2, below.

3.2. Dependence with height (z)

The evolution of the rms of some components of the quantities defined in equations (18)–(21) is shown in Figure 7, for different z . The vertical components of the velocity and magnetic fields show clear exponential growth phases. There is small, but non-negligible, variation in the growth rates calculated for varying z (with growth rates slightly smaller for low z). The reason for this variation is that, as discussed in the previous Section, these solutions do not correspond to a single unstable mode; we are not here solving the linearized problem. (And, in fact, even if we had a single mode, our background state is slowly evolving away from the initial state.) Nevertheless, these variations do not prevent a meaningful overall growth rate for the instability being calculated. The growth is clearest in the components u_z and b_z shown, as these components are most directly driven by the instability. Other variables (including s , also shown) are more subject to non-linear effects, including the mixing of different modes and the evolution of the background state. The latter is a significant effect, as the average density in the midplane ($z = 0$) at the

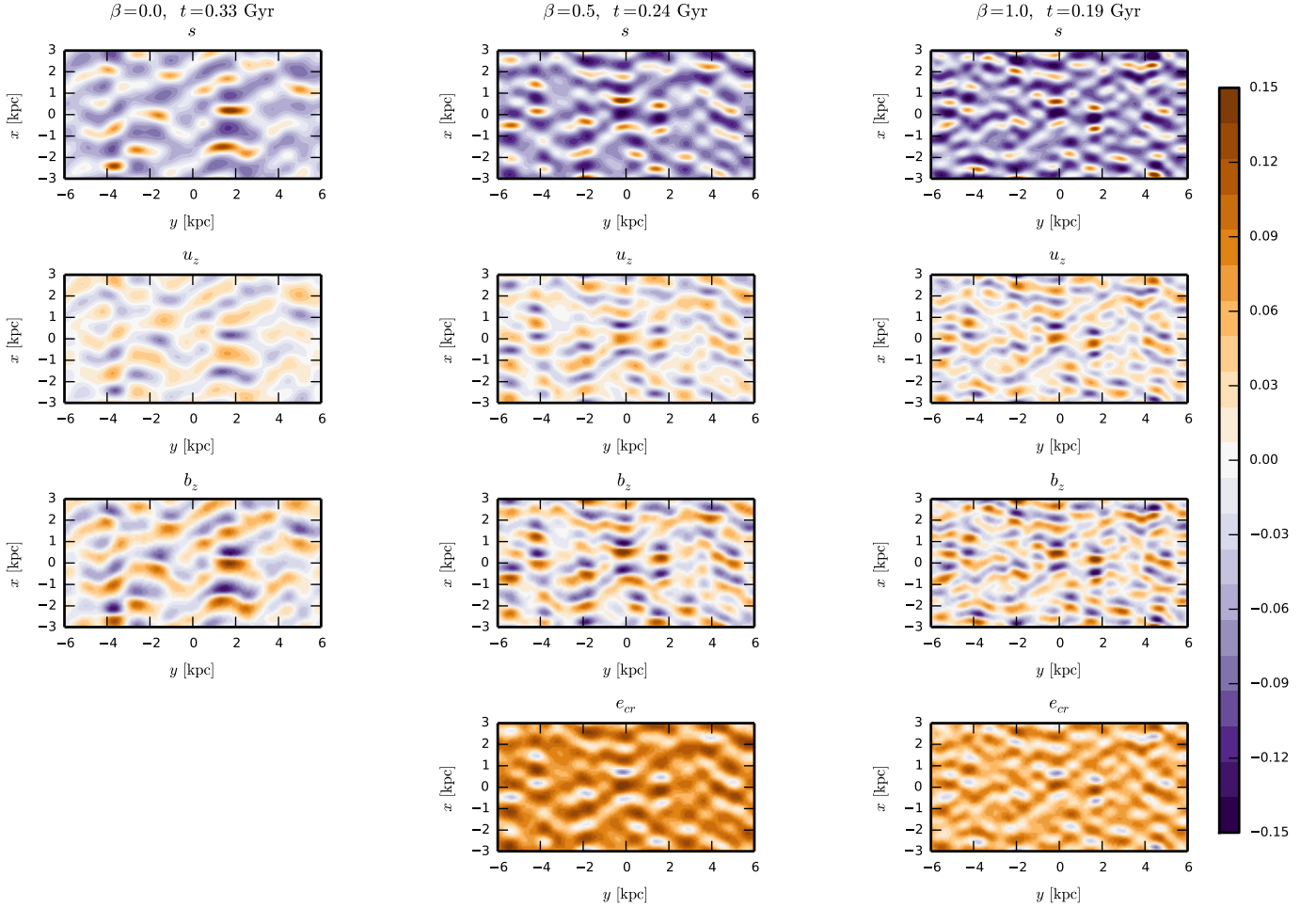


Figure 4. Slices at $z = 0.5$ kpc of the deviations to the initial density field, s , to the vertical component of the velocity field, u_z and to the magnetic field, b_z and to the cosmic rays energy density, e_{cr} . The snapshots at the instant when $E_{kin} = 0.7E_{thm}$.

time $E_{kin} = 0.7E_{thm}$ is on average 3%/5%/5% higher than the initial state for the cases $\alpha = 1$ and $\beta = 0/0.5/1$, due to the net sinking of gas produced by the Parker instability. Similarly, there is a net rise of cosmic rays, with the cosmic ray energy density at that time being 15%/11% smaller than the initial state, for $\alpha = 1$ and $\beta = 0.5/1$.

In many of the linearized analyses (e.g. [Giz & Shu 1993](#); [Kim & Hong 1998](#)), it is noted that the instabilities may possess a specific symmetry with respect to reflection in the midplane: either symmetric (the so called ‘odd’ modes, with no midplane crossings), with s , u_x , u_y , b_x , b_y and e_{cr} symmetric and u_z and b_z antisymmetric under the mapping $z \rightarrow -z$; or antisymmetric (the ‘even’ modes, allowing midplane crossings), with s , u_x , u_y , b_x , b_y and e_{cr} antisymmetric and u_z and b_z symmetric under this mapping. Note that these perturbations are with respect to the initial state, which in these terms is itself symmetric (‘odd’). For some systems, (e.g. [Horiuchi et al. 1988](#); [Basu et al. 1997](#)) it is found that the antisymmetric mode of instability is preferred; and it is notable that this allows an effective factor of two decrease in the horizontal separation of high density patches (since the antisymmetric density perturbation allows adjacent peaks in the (y, z) -plane to be at (y, z) and $(y + \lambda_y/2, -z)$; rather than at $(y, \pm z)$ and $(y + \lambda_y, \pm z)$, as for the symmetric case). This has implications for the establishment of realistic spacings in galactic density concentrations (i.e. giant molecular clouds); and also for

the timescales of evolution of these features, since the linear growth rates depend upon the wavelength. Some authors (e.g. [Basu et al. 1997](#); [Mouschovias et al. 2009](#)) consider the non-linear evolution of the most unstable pure symmetry mode.

However, [Giz & Shu \(1993\)](#), [Kim & Hong \(1998\)](#) note that for a system with a ‘realistic’ gravity profile, such as we study, the growth rates of the most unstable modes show no preference for either type of symmetry. And in any event, as the solution evolves nonlinearly (and with interaction with the symmetric initial state), the antisymmetric modes excite symmetric components, and so purely antisymmetric perturbations cannot be sustained in the nonlinear regime.

A simple visual inspection suggests that our nonlinear solutions do not exhibit either pure symmetry or antisymmetry with respect to reflection in the midplane. Note that our weak random initial velocity is asymmetric, so does not seed either pure symmetry of perturbation. Nevertheless, if one symmetry was genuinely preferred, we would expect the weak initial component of the other symmetry simply to decay. (And were a pure symmetry solution to be obtained from a pure symmetry initial condition, it could not be considered robust to the inevitable fluctuations of a real system.)

To better examine this, we studied how the magnetic energy is distributed between symmetric and antisymmetric modes. For simplicity, we restrict the analysis to the x and z components, which are zero at the start of the simulation and avoid

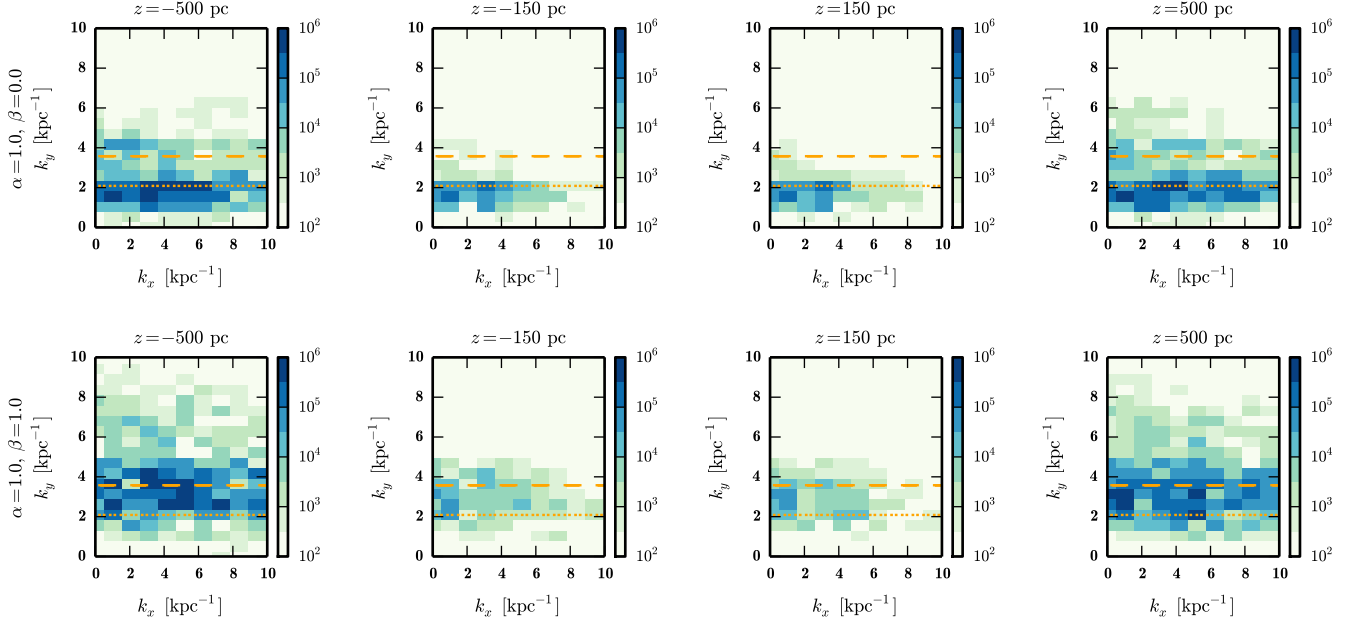


Figure 5. Two-dimensional power spectrum of $b_z = B_z/B_{y,0}$. The power spectra were computed over slices of fixed z , as indicated in each panel. The top row shows the power spectra for $\alpha = 1$ and $\beta = 0$. The bottom row shows the power spectra for $\alpha = 1$ and $\beta = 1$. Different colors correspond to different powers, as shown in the colorbar. Contour lines (drawn without taking the log) highlight major the peaks. The short- and long-dashed orange curves show the k_y associated with the fastest growing mode obtained from the calculations of [Giz & Shu \(1993\)](#) for $\alpha = 1$ and $\beta = 0, 1$, respectively.

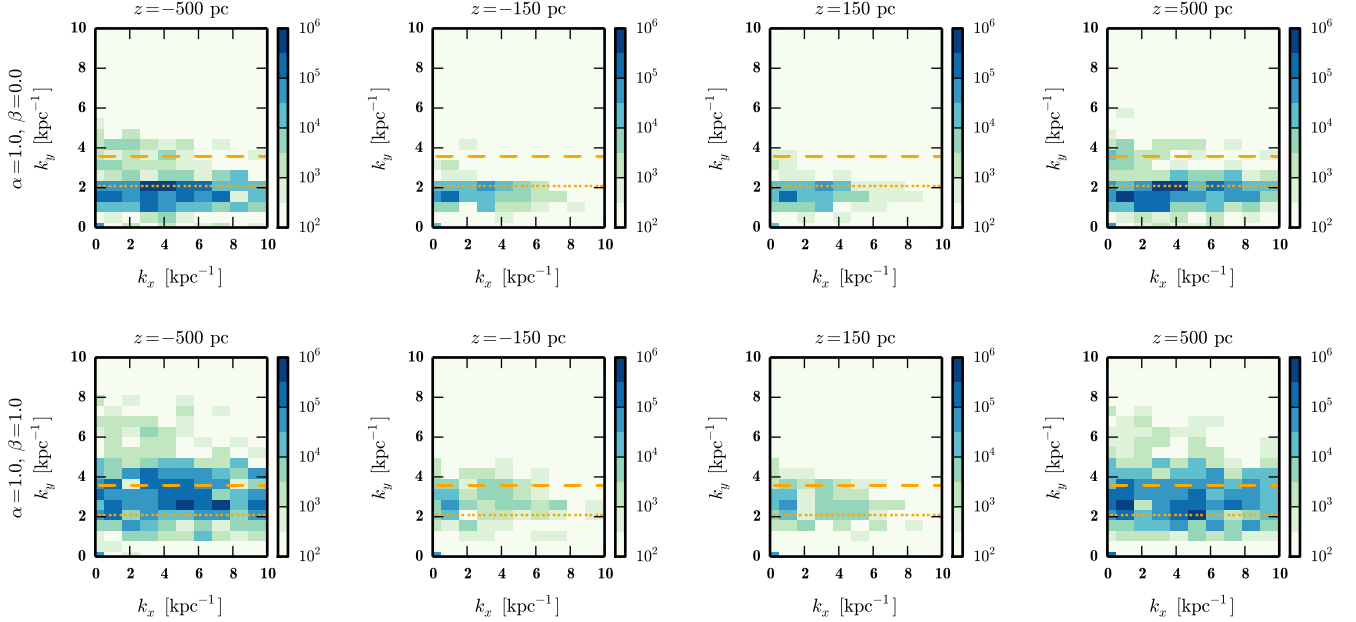


Figure 6. Same as Figure 5 but for the vertical component of the velocity perturbation, $u_z = U_z/c_s$.

the complication of the symmetry of the background state. The symmetric part is

$$B_x^{(s)}(x, y, z) = \frac{1}{2} (B_x(x, y, z) + B_x(x, y, -z)), \quad (22)$$

$$B_z^{(s)}(x, y, z) = \frac{1}{2} (B_z(x, y, z) - B_z(x, y, -z)), \quad (23)$$

and the antisymmetric,

$$B_x^{(a)}(x, y, z) = \frac{1}{2} (B_x(x, y, z) - B_x(x, y, -z)), \quad (24)$$

$$B_z^{(a)}(x, y, z) = \frac{1}{2} (B_z(x, y, z) + B_z(x, y, -z)). \quad (25)$$

From these, we compute the total energy associated with each magnetic field component, $E_{x/z}^{(s/a)} = \int (B_{x/z}^{(s/a)})^2 / 8\pi \, dV$, in the simulation domain and construct the following diagnostic

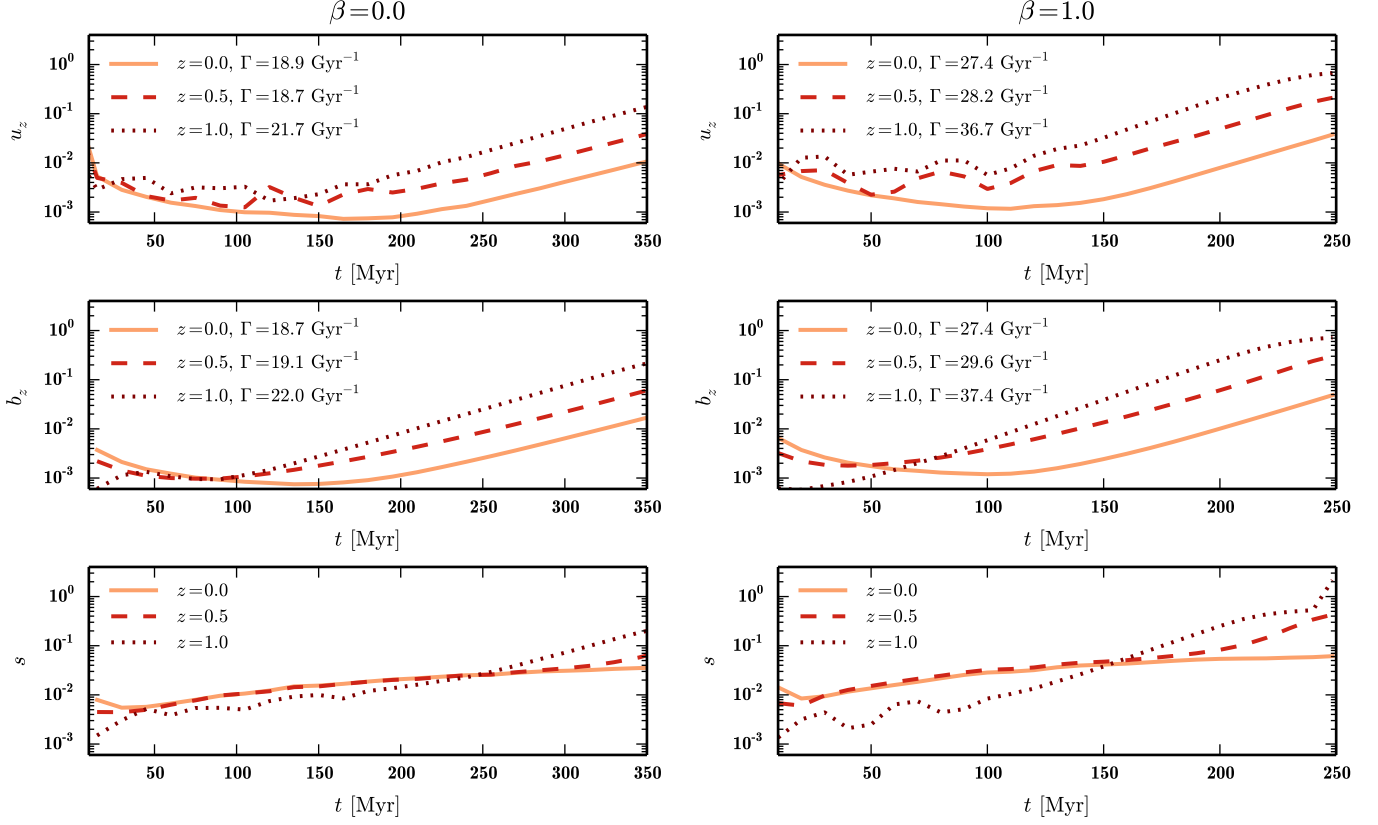


Figure 7. Root mean square evolution of the perturbations for models with $\alpha = 1$ at three different slices of fixed vertical coordinate, z , as indicated in each panel. The panels in the left column shows the results in the absence of cosmic rays, while the right-hand column shows the case of $\beta = 1$.

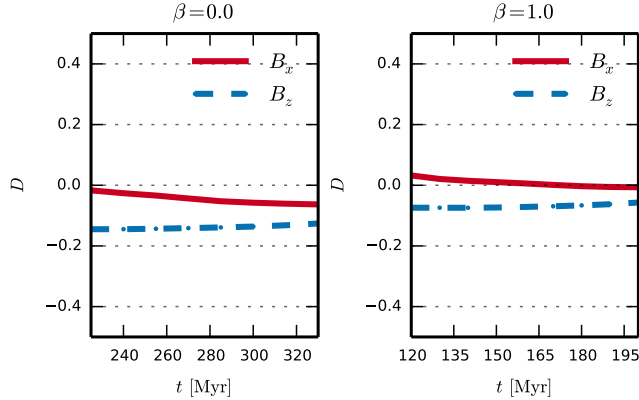


Figure 8. Time evolution of D (equation 26), in the cases of $\beta = 0$ and $\beta = 1$ (with $\alpha = 1$ in both cases). $D = 1$ indicates pure symmetry with respect to reflection in the midplane, while $D = -1$ indicates pure antisymmetry.

quantity

$$D = \frac{E_{x/z}^{(s)} - E_{x/z}^{(a)}}{E_{x/z}^{(s)} + E_{x/z}^{(a)}}. \quad (26)$$

Thus, $D = 1$ for pure symmetry or $D = -1$ for pure antisymmetry.

In figure 8, the evolution of D is shown. In the $\beta = 0$ case, there is a slight preference for antisymmetric modes ($0 > D > -0.15$). The presence of cosmic rays makes any preference even less clear.

We therefore conclude that pure symmetry with respect to reflections in the midplane should not be expected in the non-

linear case. In this respect, the situation is rather like that with the horizontal structures, noted above; in the nonlinear regime, a spectrum of modes, of differing wavenumbers (k_x, k_y) and of differing midplane-symmetries, must be expected. We note that this was appreciated by [Giz & Shu \(1993\)](#), in their discussion of continuum modes (to which our solutions should correspond; since, as noted by [Kim & Hong \(1998\)](#), these have growth rates significantly higher than the discrete modes, so must be expected to dominate). They observed that the analysis of individual modes is of limited relevance, with an initial value treatment (such as that adopted here) being more appropriate; and with the finally realised state depending on initial conditions and nonlinear effects. As [Giz & Shu \(1993\)](#) also note, however, the modal analysis remains valid with respect to conclusions about exponential growth (as confirmed by Figure 7), since we are still working with a complete set of functions.

3.3. Dependence on diffusivities (ν , η , κ_{\parallel})

The previous results were for our fiducial choices of constant kinematic viscosity $\nu_{\text{fiducial}} \approx 3.16 \times 10^{25} \text{ cm}^2 \text{ s}^{-1}$ and constant magnetic diffusivity $\eta_{\text{fiducial}} \approx 1.58 \times 10^{25} \text{ cm}^2 \text{ s}^{-1}$, corresponding to magnetic Prandtl number $\text{Pm} = \nu/\eta = 2$. The dependence of the results on these parameters was examined; in Figure 9 we compare growth rates with variations in the ranges $0.25\text{--}2 \nu_{\text{fiducial}}$ and $0.2\text{--}3 \eta_{\text{fiducial}}$. There are small increases in the growth rate, $\sim 1\text{--}2 \text{ Gyr}^{-1}$ (or $\lesssim 5\%$), when the magnetic diffusivity is decreased to $1/5$ or the viscosity is reduced to $1/4$ of the fiducial values. Conversely, increasing ν and η by factors 2 and 3, respectively, leads to decreases in the growth rate $\lesssim 10\%$. Such a decrease of the growth

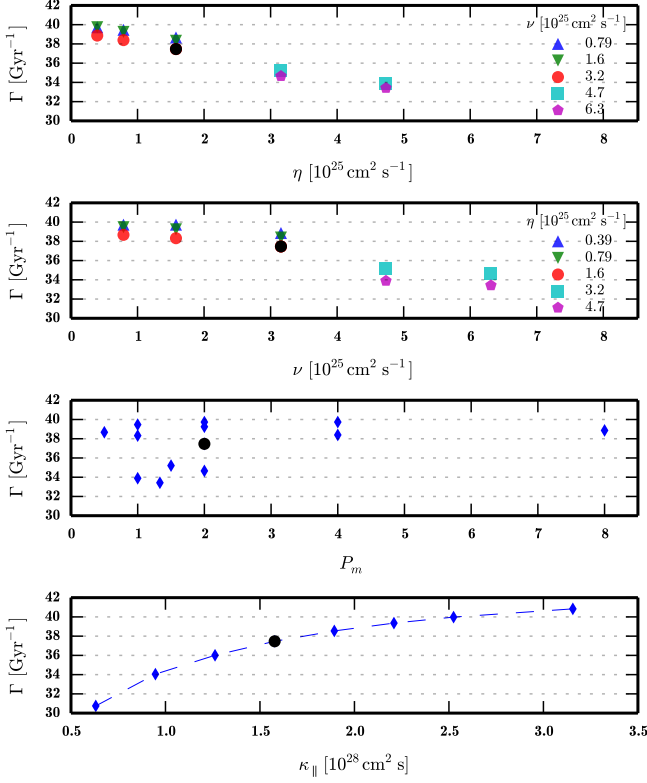


Figure 9. The dependence of the growth rate of U_{rms} in the model with $\alpha = \beta = 1$ on: the magnetic diffusivity, η ; the viscosity, ν ; the magnetic Prandtl number, P_m , and the cosmic ray diffusivity, $\kappa_{||}$. The fiducial values are shown as black circles.

rate with increasing diffusivities might be expected on energetic grounds; but the choice of diffusivities clearly has only a small effect on the growth rate, particularly when compared to its variation with α and (particularly) β .

Together, the variations with ν and η show no clear dependence on the magnetic Prandtl number in the range $P_m = 0.5$ – 8 ; as can be seen in the third panel of Figure 9. This range of course remains far from the expected values for galactic disks, $P_m \gg 1$; but along with the agreement with the ideal linearized studies, this nevertheless suggests that the instability is not strongly influenced by diffusion.

In the lowest panel of Figure 9 we show the impact on the growth rate of varying the cosmic ray diffusivity along the magnetic field, $\kappa_{||}$. In agreement with the results of Ryu et al. (2003), the difference between realistic values and even larger values (i.e. moving towards the approximation of infinite parallel diffusivity) is small: doubling the value of $\kappa_{||}$ from our fiducial value leads to a 9% increase in the growth rate. (Decreasing $\kappa_{||}$ from the fiducial value gives a slightly larger effect; but this direction is moving away from galactically reasonable values.)

3.4. Observational signatures

Having a satisfactory model where Parker instability is the dominant effect, we now look for simple possible observational signatures and their dependence on the cosmic ray content. We start by examining the archetypal signature of the Parker instability: the so-called Parker arches/loops. Naively, one would expect the loops to be present in (polarized) synchrotron intensity maps of edge-on galaxies. Thus, we show in Figure 10 polarized synchrotron intensity at $\lambda = 1$ cm (see

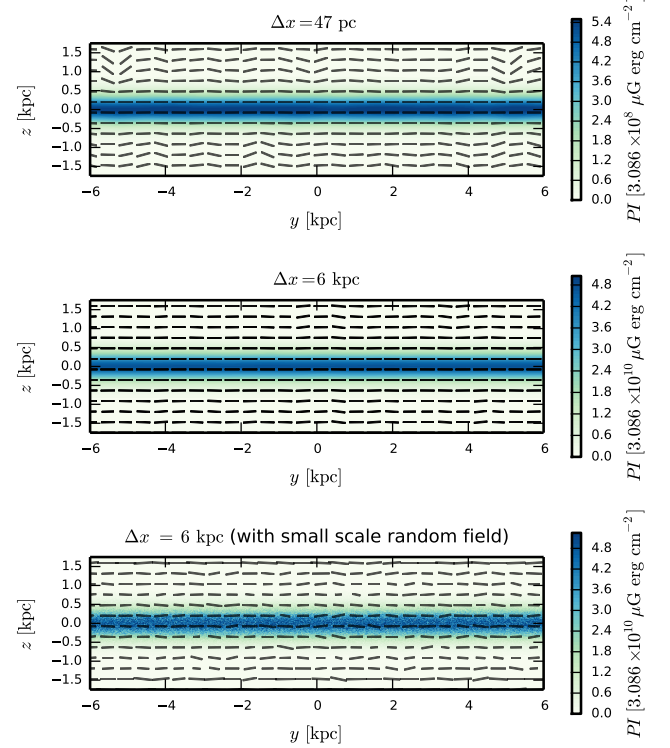


Figure 10. Polarization view of the model with $\alpha = \beta = 1$. The shaded contours in the three panels show the polarized intensity, PI , in arbitrary units; dashes are oriented perpendicularly to the angle of polarization and their lengths show the degree of polarization. For each panel, the integration was over the interval indicated above that plot. The bottom panel shows the effect of the inclusion of a gaussian random field.

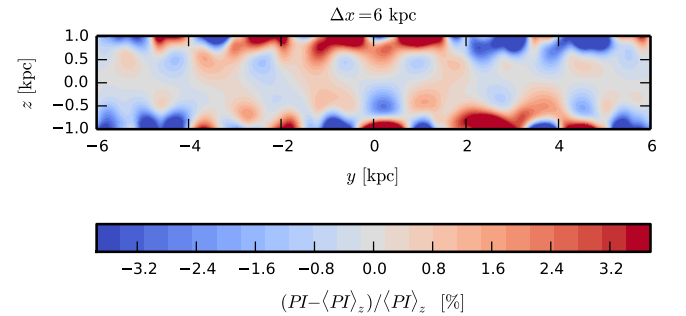


Figure 11. Fluctuations in the polarized intensity relative to the average at each z are shown, for the solution analyzed in Figure 10.

appendix B for the details of the calculation). In the top panel, which shows the result of integrating over a thin slice of width $\Delta x = 47$ pc, the polarization angles are affected by the undulations of the magnetic field lines. The polarized and total synchrotron intensities, however, are dominated by the disk stratification, and the variations at the same disk height are almost negligible. Observing an isolated thin slice of an edge-on galactic disk is not possible. Thus, in the second panel the integration is performed over the whole simulation box ($\Delta x = 6$ kpc). The undulations in the polarization angles are mostly erased and the signal in the intensity remains almost featureless. In Figure 11 the fractional difference to the average at each z is shown: a very weak signal ($\lesssim 2\%$) can be identified within one scale height from the midplane; at larger distances stronger fluctuations relative to the z -average are found ($\sim 3.5\%$). Finally, in the third panel of Figure 10,

we check the effect of the presence of a turbulent random field component, by adding to each point a gaussian random field with a root mean square value equal to the magnitude of the model field at that height z . The presence of the random field removes any remaining (weak) signal of the Parker instability in the polarization.

The prospect of obtaining direct evidence of Parker loops from this kind of synchrotron observations is further complicated by the curvature of the galaxy, which would further weaken the signal after the integration. Figure 10 also assumes the observation are made at a wavelength of 1 cm, which minimizes Faraday rotation effects.

An alternative approach is to consider the rotation measure (RM) to probe the fluctuations in the density and magnetic field produced by the Parker instability (Figure 4). Assuming the case of a face-on galaxy, the RM can be computed from

$$\phi = (0.812 \text{ rad m}^{-2}) \int \frac{n_e(z)}{1 \text{ cm}^{-3}} \frac{B_z}{1 \mu\text{G}} \frac{dz}{1 \text{ pc}}, \quad (27)$$

where n_e is the number density of electrons in the path (for simplicity, we assumed the plasma was completely ionized).

In Figure 12, Faraday maps obtained from the simulation are shown. The integration was performed over the whole domain (i.e. a distant external radio source is assumed). There are sharp peaks in the rotation measure signal, with a maximum $|\phi| \approx 85 \text{ rad}^2 \text{ m}^{-4}$ in the $\beta = 0$ case; $|\phi| \approx 74 \text{ rad}^2 \text{ m}^{-4}$ in the $\beta = 0.5$ case; and $|\phi| \approx 91 \text{ rad}^2 \text{ m}^{-4}$ in the $\beta = 1$ case. One should, however bear in mind that these amplitudes correspond to a particular choice of output time (namely, the time when $E_{\text{kin}} = 0.7 E_{\text{thm}}$) and that with the current setup no steady state is reached. More informative is the spatial distribution of the RM structures, which changes negligibly with time. In Figure 13 the structure function (SF) of the RM is plotted, computed parallel and perpendicular to the direction of the initial magnetic field (y-direction), i.e.

$$\mathcal{D}_{\parallel}(l) = \langle [\phi(x, y) - \phi(x, y + l)]^2 \rangle, \quad (28)$$

$$\mathcal{D}_{\perp}(l) = \langle [\phi(x, y) - \phi(x + l, y)]^2 \rangle. \quad (29)$$

There are systematic differences in the SFs along and perpendicular to the large scale field, and features which are dependent on β . The first peak of the SF is generally larger in the direction along the field than in the direction perpendicular to it: for $\beta = 0$, the first peak occurs at $l_{\text{peak}} \approx 1 \text{ kpc}$ for \mathcal{D}_{\parallel} , while $l_{\text{peak}} \approx 1.5 \text{ kpc}$ for \mathcal{D}_{\perp} . When β is increased, the peaks of the SF parallel to the field are shifted towards smaller scales, with $l_{\text{peak}} \approx 0.95 \text{ kpc}$ for $\beta = 1$. In the direction perpendicular to the initial field, the SF is flattened with the increase in the cosmic ray density.

In Figure 14 this is examined for varying α . There is negligible variation on the peak positions if only the magnetic field strength is varied. Although this may be surprising, it is consistent with the relatively weak effect of varying magnetic buoyancy shown in Figure 3, and again highlights the importance of incorporating cosmic rays into these studies.

4. CONCLUSIONS

We have performed a set of three-dimensional numerical simulations exploring the growth rates and length scales associated with the Parker instability, in a section of a galactic disk with realistic vertical structures, and including cosmic rays via a fluid approximation. Aiming for clarity and to avoid any bias (via unintended forcing), our system is allowed to

evolve passively from its initial state; i.e. there is no artificial maintenance of cosmic rays and magnetic fields by imposed sources. This evolution of the background state represents a slight difference from the linearized systems investigated in related analytical studies, but the evolution is very slow compared with the timescales of the Parker instability; and we differ from such studies in more fundamental ways, in any event, incorporating finite diffusivities and retaining nonlinear interactions.

Nevertheless, the growth rates and length scales we obtain — and their dependences on the model parameters — qualitatively agree well with such linearized studies. The quantitative differences can be clearly understood in terms of the differences between the models (the linearized studies being ideal, and in some cases using alternative background profiles), or simply due to the nonlinear nature of our solutions.

Our calculations invariably produce non-trivial spatial structures, significantly involving multiple modes in the instability, and with these modes being fully three-dimensional (rather than pure undular or interchange modes) and with no preference for either pure symmetry about the midplane. This underlines the importance of three-dimensional calculations, if signatures of the instability structures, for comparison with observations, are sought. And the clear effect of the cosmic rays on the growth rate and wavelengths of the instability (as seen when varying our parameter β), highlights the importance of including this ingredient of the ISM in such calculations.

Although our calculations use high values for viscous and magnetic diffusivities, in comparison with galactic disks, our investigation with varying values suggests that the instability is not being significantly affected by these diffusivities.

For simplicity, but in contrast to real galaxies, our calculations do not involve rotation. Rotation is normally found to stabilize against the Parker instability, but we note that Kim & Hong (1998) argue that this will be less the case for a cosmic ray-driven instability, cf. instabilities with purely magnetic and gas buoyancy. And preliminary runs with rotation (not reported here) confirm that the effect is minor. Similarly, our calculations do not involve rotational shear (differential rotation), which is significant in disk galaxies. Foglizzo & Tagger (1994, 1995) find differential rotation to weaken the Parker instability; the specific effects on our calculations should be considered in future work.

As a first step towards investigating the observational implications, we calculate synthetic polarized intensity and Faraday rotation measures maps from our simulations, and compute the structure functions associated with the latter. We find that it is very unlikely that radio observations of edge-on galaxies would be able to clearly detect any structures produced by the instability, because of the averaging along the line-of-sight and the masking of any signal by the presence of the random (small-scale) magnetic field. However, our results suggest there may be strong signatures in Faraday rotation measures of face-on galaxies. And our preliminary analysis suggests that, when combined with independent data about the disk scale height, the correlation scales inferred from such rotation measure maps may be a useful observational diagnostic for the cosmic ray content of galaxies.

A comprehensive study based on the present model, solely dedicated to the observational signatures of Parker instability in galaxies, is underway.

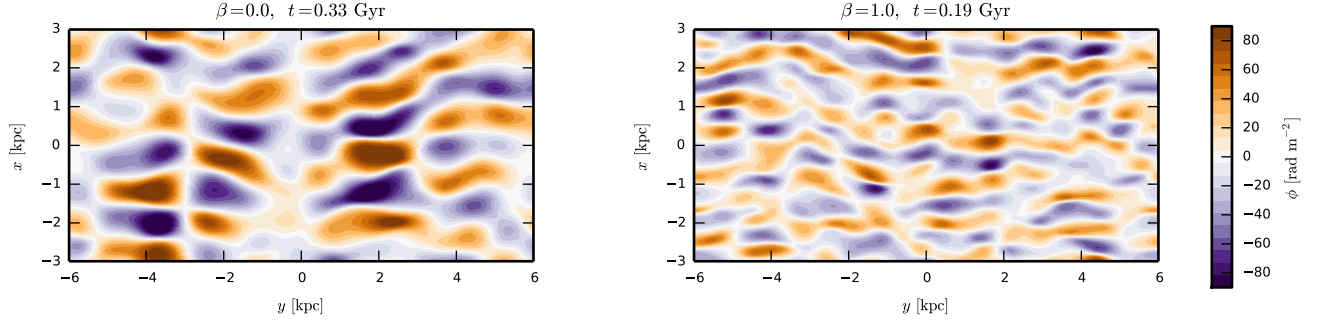


Figure 12. Faraday rotation measure maps for different β as indicated (for $\alpha = 1$), at corresponding points in the evolution of the instability (when $E_{\text{kin}} = 0.7E_{\text{thm}}$).

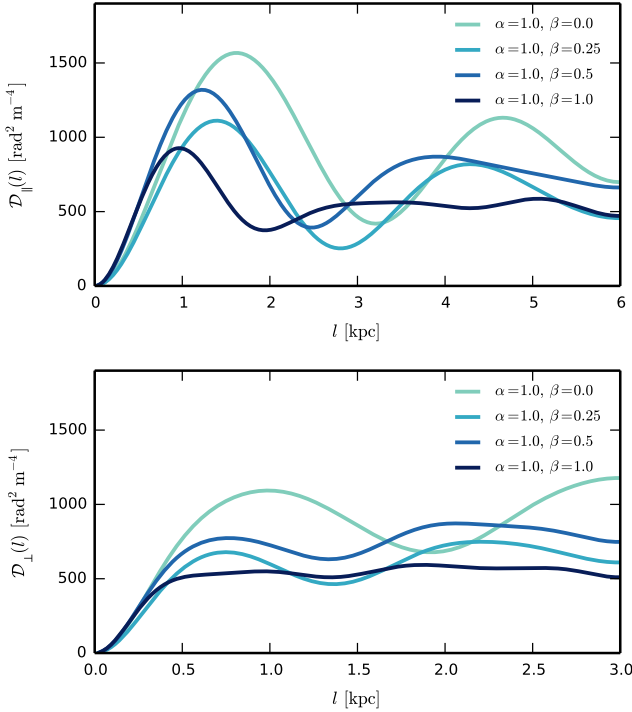


Figure 13. Structure functions computed from Faraday rotation measure maps for runs with $\alpha = 1$ and β varying as indicated in the legend. The top panel shows the structure function along the x -axis (i.e. perpendicular to the initial magnetic field) while the bottom panel shows the structure function along the y -direction.

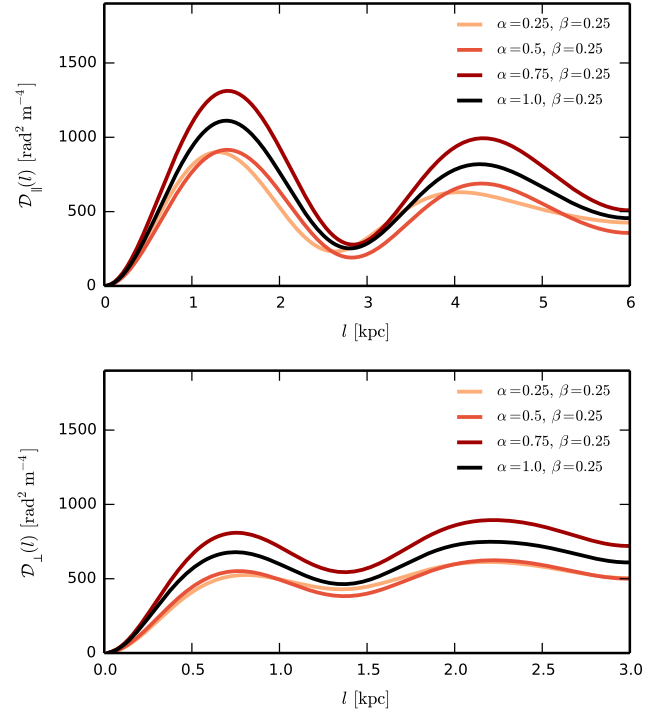


Figure 14. Structure functions computed from Faraday rotation measure maps for runs with $\beta = 0.25$ and α varying as indicated in the legend. Top panel shows the structure function along the x -axis (i.e. perpendicular to the initial magnetic field) while the bottom panel shows the structure function along the y -direction.

use of NASA's Astrophysics Data System.

ACKNOWLEDGEMENTS

We thank the referee for many constructive comments on the original version of this paper. We also thank Ann Mao for useful discussions. LFSR has been supported by STFC (grant ST/L005549/1) and acknowledges support from the European Commission's Framework Programme 7, through the Marie Curie International Research Staff Exchange Scheme LACEGAL (PIRSES-GA-2010-269264). This work was partially supported by the Leverhulme Trust (PRG-2014-427). This work made use of the facilities of N8 HPC provided and funded by the N8 consortium and EPSRC (Grant No.EP/K000225/1). The Centre is co-ordinated by the Universities of Leeds and Manchester. This research has made

APPENDIX

A. COMPARISON WITH A LARGER DOMAIN

To ensure that the vertical size of the domain is large enough to avoid boundary effects, the simulation was also run in a larger domain, with a vertical range $-3\text{ kpc} < z < 3\text{ kpc}$, which corresponds to 6 scale-heights between the midplane and the boundary (in contrast with the 3.5 scale-heights in the standard runs).

We find no significant differences between the taller simulation domain and the fiducial one. In figure 15, it can be seen that the impact on the evolution of the kinetic energy and on the rms of the velocity field is small. The growth rate of U_{rms} is, however, $\sim 6\%$ higher in the taller domain for the reasons discussed in section 3.1.

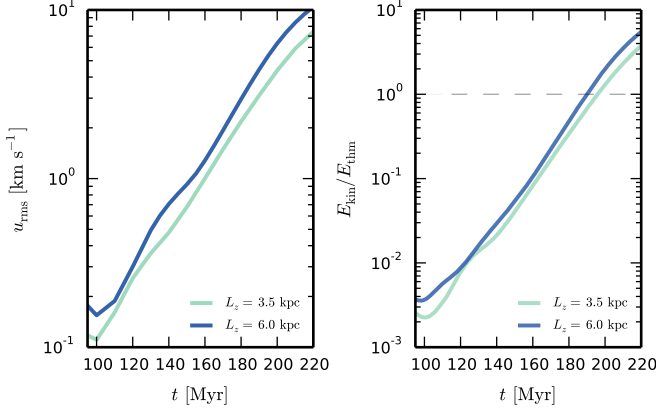


Figure 15. Evolution of the root mean square velocity (left panel) and kinetic energy (right panel), comparing the standard simulation domain, $(L_x, L_y, L_z) = (6\text{kpc}, 12\text{kpc}, 3.5\text{kpc})$, with an enlarged domain $(L_x, L_y, L_z) = (6\text{kpc}, 12\text{kpc}, 6\text{kpc})$, for $\alpha = \beta = 1$.

When comparing figure 16 with figures 5 and 6, it can be seen that the enlargement of the vertical dimension leads only to very small changes in the power spectra; and these can be attributed to small variations in the random initial conditions.

B. POLARIZATION PROPERTIES

We discuss here the details of the calculation of the polarized intensity in section 3.4.

First the Stokes parameters are computed,

$$I(y, z) = \int_0^{\Delta x} s(\mathbf{r}') dx', \quad (\text{B1})$$

$$Q(y, z) = \int_0^{\Delta x} p_0 s(\mathbf{r}') \cos[2\psi(\mathbf{r}')] dx', \quad (\text{B2})$$

$$U(y, z) = \int_0^{\Delta x} p_0 s(\mathbf{r}') \sin[2\psi(\mathbf{r}')] dx', \quad (\text{B3})$$

where the intrinsic polarization degree was assumed to be $p_0 = 0.75$, and the local polarization angle is obtained from

$$\psi(\mathbf{r}) = \frac{\pi}{2} + \arctan \left[\frac{B_z(\mathbf{r})}{B_y(\mathbf{r})} \right] + 0.81 \text{ rad} \left(\frac{\lambda}{1 \text{ m}} \right)^2 \int_x^{\Delta x} \left[\frac{n_e(\mathbf{r}')}{1 \text{ cm}^{-3}} \right] \left[\frac{B_x(\mathbf{r}')}{1 \mu\text{G}} \right] \left(\frac{dx'}{1 \text{ pc}} \right), \quad (\text{B4})$$

To compute the emissivity it was assumed that the energy density of cosmic rays is proportional to the number density of cosmic rays, thus the quantity

$$s(\mathbf{r}) = \epsilon_{\text{cr}}(\mathbf{r}) [B_y^2(\mathbf{r}) + B_z^2(\mathbf{r})]. \quad (\text{B5})$$

corresponds to the emissivity in arbitrary units.

From equations (B1)–(B3) it is then possible to compute the quantities shown in Figures 10 and 11. The polarized intensity is given by

$$PI = \sqrt{(Q^2 + U^2)}, \quad (\text{B6})$$

the observed polarization angle is

$$\Psi = \frac{1}{2} \arctan \left(\frac{U}{Q} \right), \quad (\text{B7})$$

and the polarization degree

$$p = PI/I. \quad (\text{B8})$$

REFERENCES

- Bakunin, O. G. 2008, *Turbulence and Diffusion: Scaling Versus Equations* (Springer-Verlag Berlin Heidelberg)
- Basu, S., Mouschovias, T. C., & Paleologou, E. V. 1997, *ApJ*, 480, L55
- Chou, W., Tajima, T., Matsumoto, R., & Shibata, K. 1997, *PASJ*, 49, 389
- Foglizzo, T., & Tagger, M. 1994, *A&A*, 287, 297, astro-ph/9403019
- . 1995, *A&A*, 301, 293, astro-ph/9502049
- Giz, A. T., & Shu, F. H. 1993, *ApJ*, 404, 185
- Hanasz, M., & Lesch, H. 2000, *ApJ*, 543, 235
- . 2003, *A&A*, 412, 331, astro-ph/0309660
- Hanasz, M., Otmianowska-Mazur, K., & Lesch, H. 2002, *A&A*, 386, 347
- Horiuchi, T., Matsumoto, R., Hanawa, T., & Shibata, K. 1988, *PASJ*, 40, 147
- Kim, J., & Hong, S. S. 1998, *ApJ*, 507, 254, astro-ph/9807073
- Kim, J., Hong, S. S., Ryu, D., & Jones, T. W. 1998, *ApJ*, 506, L139, astro-ph/9808244
- Kim, J., Ryu, D., & Jones, T. W. 2001, *ApJ*, 557, 464, astro-ph/0104259
- Kim, W.-T., Ostriker, E. C., & Stone, J. M. 2002, *ApJ*, 581, 1080, astro-ph/0208414
- Kuwabara, T., & Ko, C.-M. 2006, *ApJ*, 636, 290, astro-ph/0506137
- Kuwabara, T., Nakamura, K., & Ko, C. M. 2004, *ApJ*, 607, 828, astro-ph/0402350
- Kuznetsov, V. D., & Ptuskin, V. S. 1983, *Ap&SS*, 94, 5
- Matsumoto, R., Horiuchi, T., Shibata, K., & Hanawa, T. 1988, *PASJ*, 40, 171
- Matsumoto, R., Tajima, T., Shibata, K., & Kaisig, M. 1993, *ApJ*, 414, 357
- Mertsch, P., & Sarkar, S. 2013, *J. Cosmology Astropart. Phys.*, 6, 41, 1304.1078
- Mouschovias, T. C., Kunz, M. W., & Christie, D. A. 2009, *MNRAS*, 397, 14, 0901.0914
- Parker, E. N. 1966, *ApJ*, 145, 811
- . 1967, *ApJ*, 149, 517
- . 1969, *Space Sci. Rev.*, 9, 651
- . 1979, *Cosmical Magnetic Fields: their Origin and their Activity*
- Planck Collaboration et al. 2015, *ArXiv e-prints*, 1502.01582
- . 2014, *ArXiv e-prints*, 1409.6728
- Ryu, D., Kim, J., Hong, S. S., & Jones, T. W. 2003, *ApJ*, 589, 338, astro-ph/0301625
- Schlickeiser, R., & Lerche, I. 1985, *A&A*, 151, 151
- Snodin, A. P., Brandenburg, A., Mee, A. J., & Shukurov, A. 2006, *MNRAS*, 373, 643, astro-ph/0507176
- Strong, A. W., & Moskalenko, I. V. 1998, *ApJ*, 509, 212, astro-ph/9807150
- Tanuma, S., Yokoyama, T., Kudoh, T., & Shibata, K. 2003, *ApJ*, 582, 215, astro-ph/0209008
- Vidal, M., Dickinson, C., Davies, R. D., & Leahy, J. P. 2015, *MNRAS*, 452, 656, 1410.4438

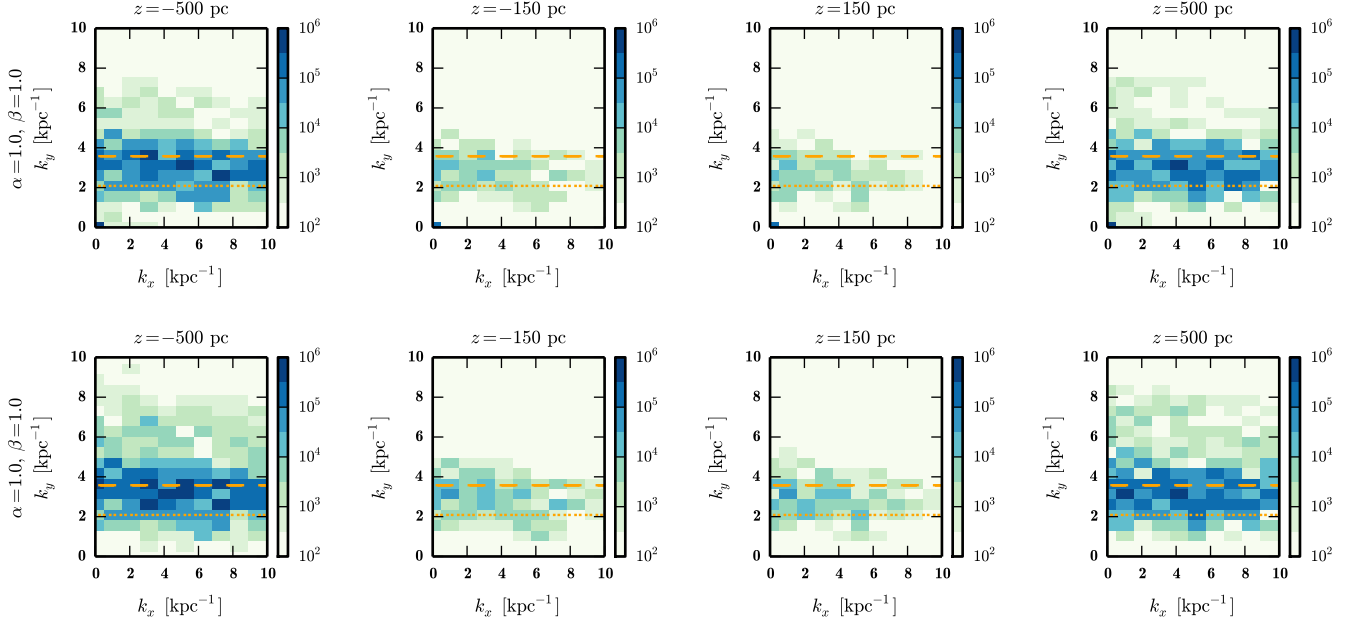


Figure 16. Two-dimensional power spectra computed for a simulation with an enlarged domain in the z -direction ($L_z = 6\text{ kpc}$), for $\alpha = \beta = 1$. The top row shows the power spectrum of $u_z = U_z/c_s$ while the bottom row shows the power spectrum $b_z = B_z/B_{y,0}$.